# Raman scattering with infrared excitation resonant with the $MoSe_2$ indirect band gap

Simone Sotgiu,[1,*] Tommaso Venanzi,[1] Francesco Macheda,[2] Elena Stellino,[3] Michele Ortolani,[1] Paolo Postorino,[1] and Leonetta Baldassarre[1,†]

[1]*Department of Physics, Sapienza University of Rome, Piazzale Aldo Moro 5, 00185, Roma, Italy*
[2]*Istituto Italiano di Tecnologia, Graphene Laboratories, Via Morego 30, I-16163 Genova, Italy*
[3]*Department of Physics and Geology, University of Perugia, Via Alessandro Pascoli, 06123 Perugia, Italy*

(Received 27 April 2022; revised 12 July 2022; accepted 27 July 2022; published 16 August 2022)

Resonance Raman scattering, which probes electrons, phonons, and their interplay in crystals, is extensively used in two-dimensional materials. Here we investigate Raman modes in $MoSe_2$ at different laser excitation energies from 2.33 eV down to the near infrared 1.16 eV. The Raman spectrum at 1.16 eV excitation energy shows that the intensity of high-order modes is strongly enhanced if compared to the first-order phonon modes' intensity due to resonance effects with the $MoSe_2$ indirect band gap. By comparing the experimental results with the two-phonon density of states calculated with density functional theory, we show that the high-order modes originate mostly from two-phonon modes with opposite momenta. In particular, we identify the momenta of the phonon modes that couple strongly with the electrons to produce the resonance process at 1.16 eV, while we verify that at 2.33 eV the two-phonon modes' line shape compares well with the two-phonon density of states calculated over the entire Brillouin zone. We also show that by lowering the crystal temperature, we actively suppress the intensity of the resonant two-phonon modes and we interpret this as the result of the increase of the indirect band gap at low temperature that moves our excitation energy out of the resonance condition.

DOI: 10.1103/PhysRevB.106.085204

## I. INTRODUCTION

Raman scattering is a widely used spectroscopic technique to study the vibrational and electronic excitations in solids. When the incoming laser energy matches a real electronic transition, in a so-called resonance effect, an enhancement of the Raman cross section occurs with respect to nonresonant processes, leading to a higher visibility of otherwise hidden modes and of high-order Raman modes, providing information on electronic transitions, phonon dispersion, and electron-phonon interaction [1–5].

Resonance Raman spectroscopy has been extensively employed to study graphene and other two-dimensional materials as it provides information on their vibrational properties [6–9] and on the presence of defects [10,11], and it is used to identify different stacking orders [12] and for growth quality check [13]. Among the vast class of two-dimensional materials, the semiconductor compounds, such as the transition metal dichalcogenides (TMDs) $MX_2$ with $M$ = Mo, W and $X$ = S, Se, Te, have attracted particular interest because of their potential applications in optoelectronic devices. The layered crystal structure, which leads to an extreme surface-to-volume ratio in the single layers, makes these materials some of the most promising candidates for the development of flexible and ultraflat optoelectronic devices [14–18].

$MoSe_2$ was shown to be attractive for several applications such as electrochemical energy storage, due to its particular chemical properties and its good conductivity [19], and as a near-infrared photodetector [20] thanks to its thickness-dependent band-gap width (indirect band gap of 1.14 eV for $MoSe_2$ bulk and 1.6 eV direct band gap for monolayers) [16,21], and its high optical absorption in the near-infrared region [22]. A deep understanding of the scattering channels, e.g., electron-phonon scattering, and of the related charge carrier transport properties [23–25] is mandatory for the implementation of TMDs in any optoelectronic device. To this end, resonance Raman scattering provides a unique possibility to address the scattering processes in $MoSe_2$ using several excitation energies, from visible to near UV [26–29]. However, to the best of our knowledge, the lowest excitation energy used was 1.58 eV; hence no Raman scattering has been reported so far with incoming photons resonant with the indirect band gap of $MoSe_2$, meaning that no study of the interaction of electrons at the bottom of the conduction band with the phonons has been performed up to now.

In this work, we present a resonance Raman scattering study of $MoSe_2$ crystals measured with an incoming photon energy of 2.33 and 1.96 eV and 1.16 eV that matches the indirect band-gap transition of $MoSe_2$. For the latter photon excitation energy we observe a great enhancement of the scattering intensity of high-order processes with respect to first-order modes. By comparing the Raman spectra with the two-phonon density of states (2ph-DOS) calculated by density functional theory (DFT), we associate these peaks with two-phonon resonant Raman processes involving the electronic transition at the indirect band gap of the crystal. Our results deepen the understanding of Raman scattering in $MoSe_2$, indicating that phonon modes with momenta

*Corresponding author: simone.sotgiu@uniroma1.it
†Corresponding author: leonetta.baldassarre@uniroma1.it

 

comparable to those connecting the indirect band-gap points in the Brillouin zone are strongly coupled to electrons. Our results, moreover, demonstrate that the near-infrared excitation radiation can be used as a powerful tool to study small-gap semiconductors obtaining relevant information on the material properties [30].

## II. METHODS

Raman spectra at 1.16 eV excitation energy are collected with a Fourier-transform (FT) interferometer (Bruker Multi-RAM), equipped with a Nd:YAG laser and a nitrogen-cooled germanium detector (spectral range 5900–11 700 $cm^{-1}$), and connected via optical fibers to an optical microscope. The spectra at room temperature are obtained with a 100× objective (numerical aperture 0.85), spectral resolution of 1 $cm^{-1}$, and a power density around 2.5 $mW/\mu m^2$. The temperature-dependent measurements are performed with a He-flow cryostat and a 4× objective. We set 2 $cm^{-1}$ resolution and 0.02 $mW/\mu m^2$ power density. The spectra at 2.33 eV and 1.96 eV excitation energy are measured with a Horiba HR Evolution microspectrometer equipped with a 100× objective coupled to a silicon CCD camera. We measure with 0.6 $cm^{-1}$ spectral resolution and power density of 5 and 0.5 $mW/\mu m^2$ for 2.33 and 1.96 eV, respectively. $MoSe_2$ single crystals are purchased from HQ Graphene. The absorbance spectrum is obtained from a transmission experiment using a Bruker FT-IR spectrometer. For DFT calculations we used a GGA-PBE functional with semiempirical Grimme-D3 van der Waals corrections [31] to optimize the geometry of the structure, employing an energy cutoff of 125 Ry and a **k**-point grid of dimensions $15 \times 15 \times 3$. The optimization leads to a lattice parameter of $a = 6.266$ bohrs and an interlayer distance of 24.665 bohrs, in accordance with [32]. The position of the electronic band gap is dependent on the interlayer distance, which is incorrectly overestimated if the van der Waals corrections are not taken in account. The 2ph-DOS—namely, $\mathrm{DOS}_{2\omega}(\epsilon) = \sum_{\mathbf{q}\mu\nu} \delta(\epsilon - \omega_{\mathbf{q}\nu} - \omega_{\mathbf{q}\mu})$, $\omega_{\mathbf{q}\mu,\nu}$ being the phonon frequency—is obtained computing the phonons using density functional perturbation theory [33] on a **q**-point grid of dimensions $6 \times 6 \times 2$, which is then interpolated on a $768 \times 768 \times 1$ grid to evaluate the sums in the expression for $D_{2\omega}(\epsilon)$. All the calculations have been performed using the QUANTUM ESPRESSO suite [34].

## III. RESULTS AND DISCUSSION

First of all we determine experimentally the energy of the indirect band gap at room temperature in order to compare it with our laser lines. We measure both the photoluminescence (PL) and the absorbance spectrum and use a Tauc procedure to extract the band-gap width [35,36] (see Fig. 1). The discrepancy between the value obtained from the PL ($E_{\mathrm{gap}}^{\mathrm{PL}} = 1.137 \pm 0.001$ eV) and the value obtained from the absorbance spectrum ($E_{\mathrm{gap}}^{\mathrm{Tauc}} = 1.16 \pm 0.02$ eV) is known as the *Stokes shift* and, in first approximation, can be explained using the Frank-Condon principle [37], but it is also modulated by strain [38], impurities [39,40], and other factors. We remark that a deeper understanding of this phenomenon in $MoSe_2$ is beyond the scope of this article; here we simply point out that our IR laser energy well matches the indirect band-gap width.

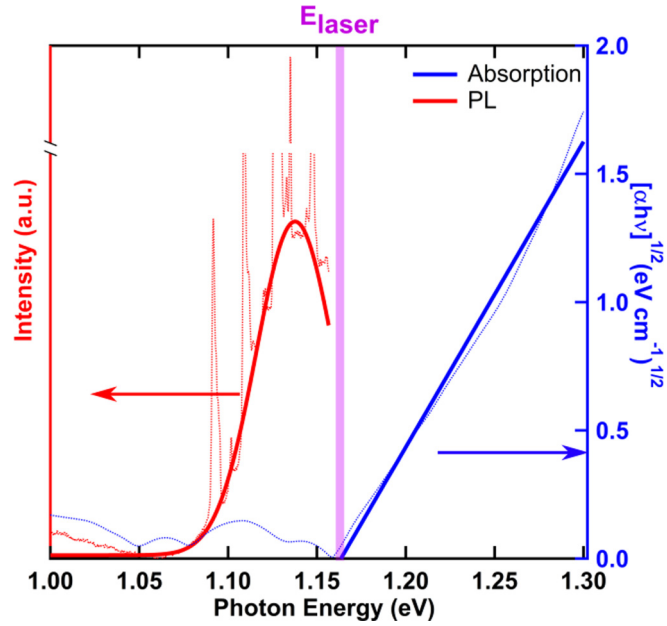


FIG. 1. Room temperature PL (red curve) obtained fitting the background of Raman spectrum $MoSe_2$ crystal (dotted red curve). The extrapolated gap is $E_{\mathrm{gap}}^{\mathrm{PL}} = 1.137 \pm 0.001$ eV. Tauc procedure (blue curve) from absorption experiment (dotted blue curve). The extrapolated gap is $E_{\mathrm{gap}}^{\mathrm{Tauc}} = 1.16 \pm 0.02$ eV. We have highlighted our 1.16 eV laser energy $E_{\mathrm{laser}}$.

### A. Raman spectra as a function of excitation energy: Experiment and theory

2*H*-$MoSe_2$ belongs to the space-group symmetry $D_{6h}^4$ and it has 12 modes of lattice vibrations at the center of the first Brillouin zone (FBZ) [26], namely,

$$\Gamma = A_{1g} + 2A_{2u} + B_{1u} + 2B_{2g} + E_{1g} + 2E_{1u} + 2E_{2g} + E_{2u}, \tag{1}$$

where $E_{1g}$, $A_{1g}$, $E_{2g}^1$, and $E_{2g}^2$ are the Raman-active modes.

Figure 2(a) shows the Raman spectra obtained at three different excitation energies. We identify three of the four first-order peaks ($E_{1g}$ at 170 $cm^{-1}$, $A_{1g}$ at 243.5 $cm^{-1}$, and $E_{2g}^1$ at 285 $cm^{-1}$). The $E_{2g}^2$ is at 32 $cm^{-1}$ and below the spectral range of our FT-Raman setup. It is worth noticing that the $E_{1g}$ mode is usually forbidden in backscattering geometry, but it is visible at 2.33 eV probably because the laser excitation energy approaches the energy of the *C* exciton (about 2.6 eV) [27,28].

We can also identify four strongly structured Raman modes, labeled as *D*, $S_1$, $S_2$, and $S_3$ in Fig. 2(a), that cannot be ascribed to first-order Raman scattering peaks. One can note that these modes are strongly enhanced in the spectrum taken at 1.16 eV, which is a signature of resonance processes [Fig. 2(b)]. Moreover, by looking at the $S_3$ mode [see Fig. 3(a)] one can note that the overall line shape is modified.

We first verify whether these are second-order Raman modes. A Stokes second-order Raman process is related to

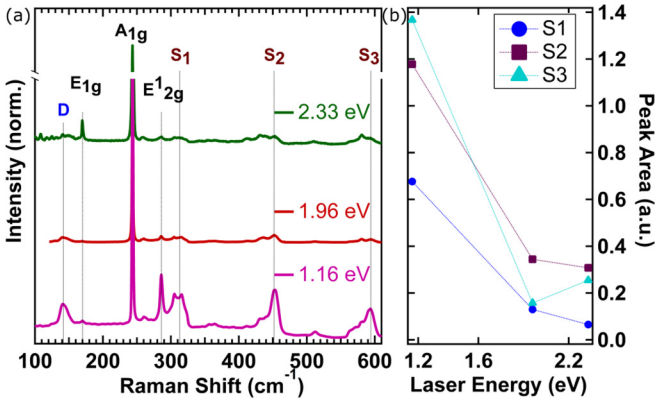


FIG. 2. (a) Spectra of $MoSe_2$ bulk taken at infrared (1.16 eV) and visible (1.96 and 2.33 eV) energies. We can observe the presence of the first-order Raman peaks (labeled in black) and high-order modes due to difference (labeled in blue) or summation (labeled in red) processes (see main text for their definition). The high-order Raman peaks in the spectrum taken at 1.16 eV are strongly enhanced. The $E_{1g}$ peak becomes visible as the excitation energy approaches the energy of the $C$ exciton (2.6 eV). All the spectra are normalized at the intensity of the $A_{1g}$ mode and vertically shifted for the sake of clarity. (b) Integrated area of the $S$ Raman features, normalized to the area of the $A_{1g}$ peak for the different laser energies used. One can clearly see the intensity enhancement of the $S$ modes with respect to first-order Raman peaks.

the creation of two phonons or to the creation of one phonon and the destruction of another [41]. The resulting Raman shift will be $\hbar(\omega_1 \pm \omega_2)$, where $\hbar\omega_{1,2}$ indicates the energy of the phonons and the sign is associated with creation and destruction of the phonon. One should recall that in a two-phonon process, the momentum conservation is achieved by imposing that the two phonons have opposite momentum and therefore no scattering with defects is required. Thus phonons in the entire FBZ are observable with Raman spectroscopy as long as the momentum is conserved and the nonresonant second-order Raman spectra map the two-phonon density of states, as shown for example in diamond [42].

We calculate the phonon dispersion [Fig. 3(b)] and the 2ph-DOS (see methods section), in order to assign the phonon branches that could be involved in two-phonon scattering processes. We compare the spectrum taken with 2.33 eV photon energy with the 2ph-DOS integrated over the entire FBZ. Even without considering the matrix elements for electron-phonon and electron-light interaction, we find a striking similarity for both the energy position and the line shape between the theoretical calculations and the experimental $S_3$ features [see Fig. 3(a), upper curves]. This excellent line shape agreement strongly suggests that at least the $S_3$ mode is due to two-phonon processes only and that using an excitation energy of 2.33 eV we do not select resonantly phonons with a specific momentum but phonons from the entire FBZ contribute equally. Therefore, we assign the $S_3$ mode to the sum of two phonons with opposite momenta from the $B_{2g}$, $A_{2u}$, $E_{2g}$, and $E_{1u}$ optical phononic branches [see Fig. 3(b)]. The second-order $S_3$ mode in Fig. 3(a), taken at 1.16 eV, shows a different line shape. This demonstrates that there are resonant processes occurring and that not all the regions in the FBZ contribute equally in the Raman cross section. Hence, we ascribe the enhancement and the modification in the line shape of these high-order modes obtained at 1.16 eV excitation energy to the processes resonant with the indirect band gap, as was seen previously in Si and GaP [43]. Our DFT calculations [Fig. 3(c)] confirm that the maximum of the valence band is located at $\mathbf{\Gamma}$, while the minimum of the conduction band lies on a point, which we will call $\mathbf{T}$, which is $\mathbf{T} = \frac{t}{3}\mathbf{b_1} + \frac{t}{3}\mathbf{b_2}$, with $t = 0.55$ and $\mathbf{b_1}$ and $\mathbf{b_2}$ the reciprocal lattice vectors, and it is situated along the $\mathbf{\Gamma}$-$\mathbf{K}$ line, in accordance with previous works [21,32,44]. We can thus depict the resonant process as the following: An electron from the top of the valence band is excited and then scattered by a phonon with a wave vector $\mathbf{q}^* \sim \mathbf{T}$, which allows the transition to the conduction band minimum. Then, a second phonon with opposite wave vector $-\mathbf{q^*}$ brings the electron to the starting point of the FBZ and then it can relax radiatively emitting a photon [see Fig. 3(c)]. The above description can be summarized with the vanishing of the second denominator in the following expression for the intensity of the Raman process [43]:

$$I \propto \left| \sum_{\mathbf{k}} \frac{\langle v|\mathbf{P}|c\rangle\langle c|H_{ep}^{(1)}|c'\rangle\langle c'|H_{ep}^{(1)}|c\rangle\langle c|\mathbf{P}|v\rangle}{\left[E_g^D(\mathbf{k}) - \hbar\omega_L\right]\left[E_g^{ID}(\mathbf{k}+\mathbf{q}^*) + \hbar\omega_\mu(\mathbf{q}^*) - \hbar\omega_L\right]\left[E_g^D(\mathbf{k}) + \hbar\omega_\mu(\mathbf{q}^*) + \hbar\omega_\nu(-\mathbf{q}^*) - \hbar\omega_L\right]} \right|^2, \tag{2}$$

where the summation runs over the FBZ wave vectors, $\hbar\omega_L$ is the laser energy, $\langle v|\mathbf{P}|c\rangle$ is the momentum matrix element between the conduction band minimum and the valence band maximum at the $\mathbf{\Gamma}$ point, separated by an energy of $E_g^D(\mathbf{k})$, and $H_{ep}^1$ is the electron-phonon Hamiltonian connecting the two states at $\mathbf{k}$ and $\mathbf{k}+\mathbf{q}^*$, separated by the energy of the indirect band-gap $E_g^{ID}(\mathbf{k}+\mathbf{q}^*)$, $\mu$ and $\nu$ being the phonon branches. As can be seen from the formula above, the Raman processes are strongly enhanced if they involve phonons with opposite momenta $\mathbf{q^*}$ and the denominator vanishes, i.e., $[E_g^{ID}(\mathbf{k}+\mathbf{q}^*) + \hbar\omega_p(\mathbf{q}^*) - \hbar\omega_L] = 0$. We remark that there are other possible resonant scattering pathways that include scattering with one electron and one hole (or with two holes). Since we assume constant matrix elements these processes are all equivalent.

In order to qualitatively understand which phonons contribute to the resonance process, we restrict the sum for $\mathrm{DOS}_{2\omega}(\epsilon)$ to a small neighborhood of $\mathbf{q^*}$ and compare the result with the spectrum taken at IR excitation energy [Fig. 3(b), lower curves]. As can be easily seen, by restricting the calculation of the 2ph-DOS at the particular wave vector $\mathbf{q^*}$, the spectral weight of the modes strongly changes, obtaining a qualitative agreement with the experimental spectrum at 1.16 eV. The 2ph-DOS does not match exactly the spectrum,

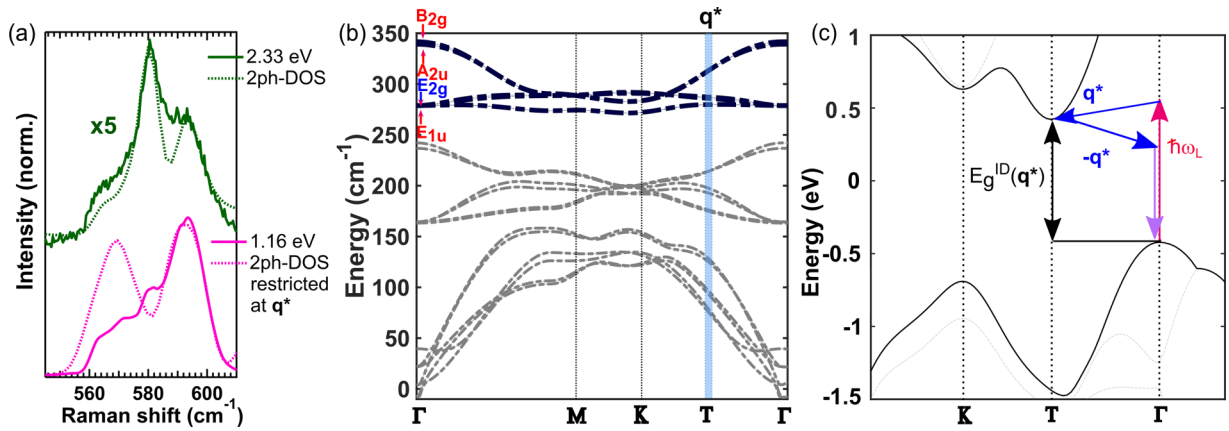


FIG. 3. (a) Raman spectra of $S_3$ modes compared with the 2ph-DOS. Besides the enhancement of the Raman scattering by using near-infrared excitation, the line shape of the peaks varies by changing the excitation laser energy revealing a resonant process. The spectra are normalized to the intensity of the $A_{1g}$ mode. (b) Phonon dispersion of bulk $MoSe_2$ restricted to the FBZ along the **Γ**-**M**-**K**-**Γ** line. The **T** point, i.e., the minimum of the conduction band, is highlighted, together with the phonon wave vector which allows the indirect electronic transition. The $S_3$ feature is then obtained as the direct sum of phonon branches highlighted in black, its energy being hence the sum of the energy of the two branches restricted to a neighborhood of **T**. In red are denoted the IR-active modes, in blue those Raman active. (c) Scheme of the resonant process described in this work: two phonons with opposite momenta can allow the indirect transition making the Raman process resonant. Note that the value of the energy gap is slightly underestimated by our DFT results, which is a typical feature of these calculations [17].

since a complete knowledge of the matrix elements in Eq. (2) would be needed, but this would fall beyond the scope of this paper. The qualitative agreement between calculation and experimental spectrum at 1.16 eV is a clear indication that the $S_3$ modes mostly originate from the depicted process. We note that a slight horizontal shift, around 5 $cm^{-1}$, was necessary to match the 2ph-DOS and the experimental spectra, due to possible DFT errors. Indeed slight changes to the lattice parameters and anharmonic effects can, for instance, have different effects on phonon frequencies in different zones of the FBZ, therefore resulting in overall shifts that may even be different for the total and restricted 2ph-DOS.

In previous studies in the literature [27,28,45–50], high-order mode assignments have been proposed, mostly linking the high-order peaks to LA modes at the **M** point, by following the criteria that flat phonon dispersions favor defect-assisted scattering processes. Here, by comparing our 2ph-DOS to the experimental curves, we can revise such assignment for some of the high-order modes.

The $S_1$ modes both for 2.33 eV [see Fig. 4(a)] and 1.16 eV [see Fig. 4(b)] excitation laser energy have a similar line shape to that of the calculated 2ph-DOS. In our calculations all the possible phonon pairs whose energy summed is 310 $cm^{-1}$ are considered (e.g., $A_{1g} + E_{2g}$ or also $B_{2g} + E_{1g}$ and so on), suggesting that several possible processes build up this peak. Notably, from the 2ph-DOS restricted at **q***, a peak around 285 $cm^{-1}$ is evident [see Fig. 4(b)] and could explain why we observe an intense $E^1_{2g}$ peak, with respect to what was measured in previous works [28]. In fact, the $E^1_{2g}$ mode was shown to be resonant with the $C$ exciton (∼2.6 eV) and to disappear completely for lower excitation energies [28]. We suppose that in our measurements at 1.16 eV excitation energy, this mode is enhanced by the underlying two-phonon resonant process occurring at the same energy.

The 2ph-DOS does not reproduce the $S_2$ modes very well. Besides a strong shift in the absolute energy (see Supplemental Material (SM) [51], Sec. A), there is no clear match in the line shapes: A reasonable agreement can be seen between

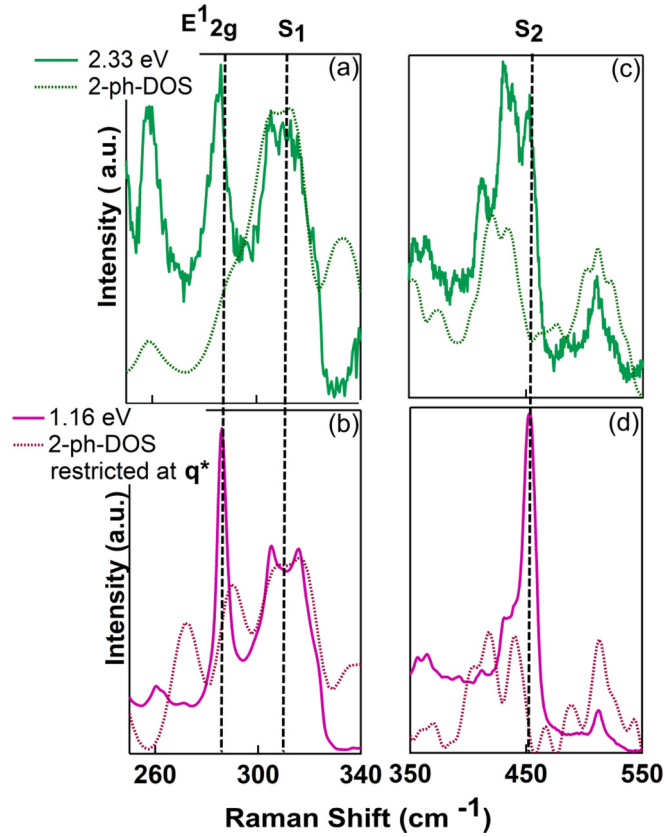


FIG. 4. (a), (b) Comparison between the spectrum taken at 2.33 eV and the 2ph-DOS integrated over all the FBZ for different Raman shift ranges. (c), (d) Comparison in the same spectral ranges for the spectrum taken at 1.16 eV and the 2ph-DOS restricted at **q***.

the 2ph-DOS and the experimental spectrum at 2.33 eV; in particular the feature around 520 $cm^{-1}$ is very well reproduced [Fig. 4(c)], while several differences can be found in the comparison between the restricted 2ph-DOS and the 1.16 eV Raman spectrum [Fig. 4(d)]. Furthermore, we had to add a shift of 20 $cm^{-1}$ to the calculated DOS in order to match the data. This is an indication that, on the one hand, the $S_2$ modes could originate by modes with more than two phonons [27] that are not considered in our calculation or, on the other hand, that one should implement in the theory the matrix elements to better evaluate the 2ph-DOS or even that the energy of the phonon branches at the edges of the FBZ could be underestimated by our DFT calculations. We note that we could not find any experimental data of the phonon dispersion in the literature, i.e., no neutron or x-ray scattering experiments, and we could not compare the DFT-calculated phonon dispersion with any data. We also note that we do not observe any peaks for Raman shifts above 600 $cm^{-1}$, suggesting that modes with order higher than two are not strong and are below our noise level.

In the literature the $D$ peak has been assigned to an $E_{2g}$-LA difference mode, enhanced by a process resonant with the $A$ exciton at 1.6 eV [28]. Even if 1.16 eV excitation energy is far from the $A$-exciton resonance, we still observe an enhancement of the $D$ mode around 148 $cm^{-1}$. The enhancement could originate from a process similar to the one discussed above for the $S$ modes. We notice also that similar resonant processes to those discussed in this paper for bulk $MoSe_2$ can be observed in monolayers for higher excitation energies. For example by measuring at 1.96 eV monolayer $MoSe_2$ we find a strong enhancement of $S$-like modes (see SM [51], Sec. B); however since therein several possible scattering processes can occur, the identification of a single resonant pathway is not easily achievable.

### B. Temperature dependence of Raman peaks

Further proof of the resonant origin of our $S$ modes could be provided with temperature-dependent measurements. Indeed, it was recently shown that the indirect band gap of bulk $MoSe_2$ increases by about 100 meV with lowering the temperature [52]. We thus aim to further demonstrate the resonant origin of the $S$ modes by driving the sample out of resonance with external temperature. In Fig. 5(a), we report the Raman spectra collected with 1.16 eV excitation energy between 15 K and 450 K. We see that the dominant effect of lowering the temperature is the strong reduction of the intensity of the $S$ and $D$ modes. In particular, the spectral feature $D$ completely disappears at 15 K, while all the other second-order modes are only reduced as the temperature is lowered. Figure 5(b) shows the PL emission between 150 K and 450 K. We note that the data show an increase of the PL intensity and a redshift of the correspondent band center with temperature, suggesting that in this temperature range the indirect electronic transition can be accomplished with the infrared laser energy used; this leads to the vanishing of the second denominator in Eq. (2), meaning that the resonance condition is still fulfilled. What we can notice is that a minor peak at 360 $cm^{-1}$ Raman shift gains spectral weight by increasing the temperature above 350 K and that the line shapes of $S_1$ and $S_3$ modes are modified. We

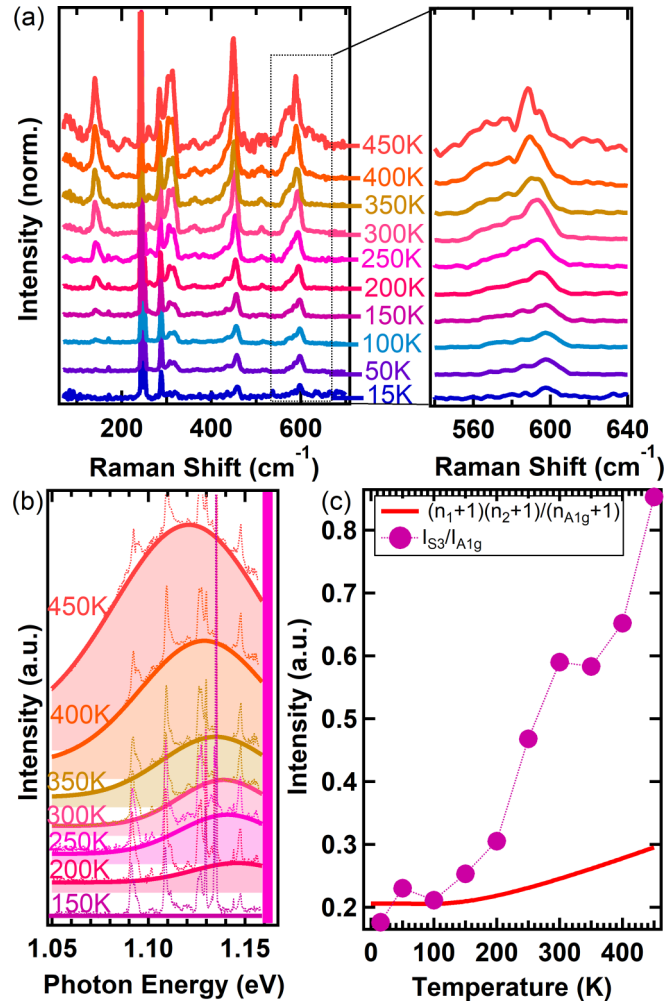


FIG. 5. (a) Temperature-dependent Raman spectra of $MoSe_2$ taken at 1.16 eV plotted between 100–700 $cm^{-1}$ and a zoom of the $S_3$ modes. The PL background has been subtracted from the spectra that are then normalized to the $A_{1g}$ peak. Spectra have been offset for the sake of clarity. (b) PL peak as extracted from Raman measurements for several temperatures indicated in figure. We observe a PL emission between 200 K and 450 K suggesting that in this temperature range we are able to reach the conduction band minimum through an indirect electronic transition; hence the resonance condition is fulfilled for the second-order Raman process described above. The vertical line represents the laser energy. (c) Comparison between the thermal occupancy given by the BE statistics and the ratio of the $S_3$ modes and the $A_{1g}$ peak. We used the values $\hbar\omega_1 = 310$ $cm^{-1}$ and $\hbar\omega_2 = 286$ $cm^{-1}$, as explained in the main text. The BE curve has been multiplied for a constant so to match the values of the experimental points at low temperature (i.e., to the average of the $I_{S3}/I_{A1g}$ value of the three points below 100 K where there is no PL peak, hence no resonance condition).

can interpret this as a result of the reduction of the indirect band gap, which thus allows for extra scattering pathways in $MoSe_2$. Indeed, only by means of thermal occupation we would not expect a modification of the line shape.

First of all we consider the temperature dependence of the Raman intensities arising from the Bose-Einstein (BE) statistical occupation. A Stokes process, with an energy shift

of $\hbar\omega_1$, has a temperature dependence of $[n(\omega_1, T) + 1]$, where $n(\omega_1, T) = (e^{\hbar\omega_1/k_B T} - 1)^{-1}$ is the BE factor, $T$ being the temperature of the crystal and $k_B$ the Boltzmann constant. For a two-phonon process, we must consider the product $[n(\omega_1, T) + 1][n(\omega_2, T) + 1]$, where $\hbar\omega_1$ and $\hbar\omega_2$ are the energies of the two phonons involved [41,53]. At each temperature, a fitting procedure has been applied to $A_{1g}$ and higher-order modes using a multi-Gaussian plus a linear function baseline (see SM [51], Sec. C, for the fit procedure). We divide the intensity obtained from the fit of the higher-order modes to the corresponding intensity of the $A_{1g}$ peak and we compare the results with the BE ratio $[n(\omega_1, T) + 1][n(\omega_2, T) + 1]/[n(\omega_{A_{1g}}, T) + 1]$.

Figure 5(c) shows the temperature dependence of the BE statistics for a two-phonon process and the experimental intensity ratios for the $S_3$ mode (see SM [51], Sec. D, for more details about the BE trend). We used the values $\hbar\omega_1 = 310$ cm$^{-1}$ and $\hbar\omega_2 = 286$ cm$^{-1}$ for estimating the theoretical trend. These are intended to be only qualitative values extracted from the phonon dispersion around **T** for the high-energy optical phonon branches [Fig. 3(b)] with the constraint that $\hbar\omega_1 + \hbar\omega_2$ should be equal to 596 cm$^{-1}$, the central energy of the most intense $S_3$ peak. Our intent was not to assign unequivocally the phonons involved but only to show that the experimental trend and the thermal one differ strongly in the measured temperature range. In Fig. S4 of the Supplemental Material [51] we plot the ratio $(n_1 + 1)(n_2 + 1)/(n_{A1g} + 1)$ for different energy values of the two phonons involved, always with the condition that $\hbar\omega_1 + \hbar\omega_2 = 596$ cm$^{-1}$. The curves are barely distinguishable, meaning that the particular values used for the BE statistics, under the aforementioned conditions, do not affect the analysis.

The $D$ feature vanishes at low temperature, as expected by the temperature dependence of the BE ratio for phonons originating from a difference of two modes (see SM [51], Sec. D). In fact, at low temperatures there are no phonons to be taken from the system, or, in other words, the system cannot be cooled by phonon absorption.

The hampering of the $S$ Raman modes cannot be described with the reduction of the phonon occupancy only but also with the thermally driven increase of the band gap that drives our excitation energy out-of-resonance (see Fig. 5(b) for the $S_3$ mode and SM [51], Sec. D, for the other modes). We note that we neglect the possible contribution of anharmonic effects in reducing the Raman peak intensity.

## IV. CONCLUSIONS

In conclusion, we have investigated Raman spectra of bulk $MoSe_2$ crystals using visible (1.96 and 2.33 eV) and near-infrared (1.16 eV) excitation energies. In the latter case, we have found a significant increase in the intensity of second-order Raman modes. We have attributed this enhancement to a Raman process resonant with the indirect band gap of the crystal. We have compared the second-order Raman spectra with the two-phonon density of states calculated using a DFT approach. We have found good agreement between the Raman spectra measured with 2.33 eV excitation energy and the two-phonon density of states integrated over the entire FBZ. This demonstrates that (i) most of the high-order features can be ascribed to two-phonon resonances and that (ii) at this photon energy the second-order Raman spectrum is not resonant with any specific indirect electronic transition with momentum away from zero. Differently, by using near-infrared excitation energy, the two-phonon Raman spectrum shows a qualitative agreement with the two-phonon density of states restricted to **q***, i.e., the wave vector of the indirect electronic transition, further indicating that this process is resonant with the $MoSe_2$ indirect band gap. To further corroborate this result, we have measured Raman spectra as a function of the sample temperature. By comparing the intensity variation of the Raman modes with the thermal statistic of phononic occupation, we have ascribed the peak intensity decrease to a thermally driven out-of-resonance condition due to the increase of the band-gap energy at low temperatures.

Understanding Raman scattering is of primary importance for different applications, such as growth quality control or individuation of $MoSe_2$ minerals, and gives a valuable insight on the phonon dispersion and its coupling with electrons at the bottom of the conduction band [54]. This study broadens the understanding of the resonance Raman spectrum in $MoSe_2$ and shows that Raman scattering with near-infrared excitation energy is a very important complementary tool for the study of van der Waals semiconductors. In perspective, we envision that one could make use of a near-infrared tunable laser to probe the phonon dispersion away from zone center by means of resonance Raman scattering in small-gap semiconductors.

## ACKNOWLEDGMENTS

The authors thank Lorenzo Graziotto and Francesco Mauri for helpful and friendly discussions. We acknowledge the European Union's Horizon 2020 research and innovation program under Grant Agreement No. 881603-Graphene Core3. We acknowledge support from the PRIN2017 Grant No. 2017Z8TS5B. We acknowledge that the results of this research have been achieved using the DECI resource Mahti CSC based in Finland [55] with support from the PRACE aisbl. We also aknowledge PRACE for awarding us access to Juliot-Curie at TGCC, France.

[1] M. Cardona and R. Merlin, *Light Scattering in Solids IX*, Topics in Applied Physics (Springer, Berlin, 2007), Vol. 108.

[2] P. Brüesch, *Phonons: Theory and Experiments II: Experiments and Interpretation of Experimental Results* (Springer Science & Business Media, 2012).

[3] B. R. Carvalho and M. A. Pimenta, Resonance Raman spectroscopy in semiconducting transition-metal dichalcogenides: Basic properties and perspectives, 2D Mater. **7**, 042001 (2020).

[4] J.-U. Lee and H. Cheong, Resonance Raman effects in transition metal dichalcogenides, J. Raman Spectrosc. **49**, 66 (2018).

[5] M. Placidi, M. Dimitrievska, V. Izquierdo-Roca, X. Fontané, A. Castellanos-Gomez, A. Pérez-Tomás, N. Mestres, M. Espindola-Rodriguez, S. López-Marino, M. Neuschitzer *et al.*,

Multiwavelength excitation Raman scattering analysis of bulk and two-dimensional $MoS_2$: Vibrational properties of atomically thin $MoS_2$ layers, 2D Mater. **2**, 035006 (2015).

[6] L. Malard, M. A. Pimenta, G. Dresselhaus, and M. Dresselhaus, Raman spectroscopy in graphene, Phys. Rep. **473**, 51 (2009).

[7] A. C. Ferrari, J. C. Meyer, V. Scardaci, C. Casiraghi, M. Lazzeri, F. Mauri, S. Piscanec, D. Jiang, K. S. Novoselov, S. Roth *et al.*, Raman Spectrum of Graphene and Graphene Layers, Phys. Rev. Lett. **97**, 187401 (2006).

[8] S. Caramazza, A. Collina, E. Stellino, F. Ripanti, P. Dore, and P. Postorino, First- and second-order Raman scattering from $MoTe_2$ single crystal, Eur. Phys. J. B **91**, 35 (2018).

[9] R. Saito, Y. Tatsumi, S. Huang, X. Ling, and M. Dresselhaus, Raman spectroscopy of transition metal dichalcogenides, J. Phys.: Condens. Matter **28**, 353002 (2016).

[10] A. Eckmann, A. Felten, A. Mishchenko, L. Britnell, R. Krupke, K. S. Novoselov, and C. Casiraghi, Probing the nature of defects in graphene by Raman spectroscopy, Nano Lett. **12**, 3925 (2012).

[11] Z. Wu and Z. Ni, Spectroscopic investigation of defects in two-dimensional materials, Nanophotonics **6**, 1219 (2017).

[12] C. Cong, T. Yu, K. Sato, J. Shang, R. Saito, G. F. Dresselhaus, and M. S. Dresselhaus, Raman characterization of ABA- and ABC-stacked trilayer graphene, ACS Nano **5**, 8760 (2011).

[13] M. O'Brien, N. McEvoy, D. Hanlon, T. Hallam, J. N. Coleman, and G. S. Duesberg, Mapping of low-frequency Raman modes in CVD-grown transition metal dichalcogenides: Layer number, stacking orientation and resonant effects, Sci. Rep. **6**, 19476 (2016).

[14] T. Mueller and E. Malic, Exciton physics and device application of two-dimensional transition metal dichalcogenide semiconductors, npj 2D Mater. Appl. **2**, 29 (2018).

[15] Q. H. Wang, K. Kalantar-Zadeh, A. Kis, J. N. Coleman, and M. S. Strano, Electronics and optoelectronics of two-dimensional transition metal dichalcogenides, Nat. Nanotechnol. **7**, 699 (2012).

[16] P. Tonndorf, R. Schmidt, P. Böttger, X. Zhang, J. Börner, A. Liebig, M. Albrecht, C. Kloc, O. Gordan, D. R. Zahn *et al.*, Photoluminescence emission and Raman response of monolayer $MoS_2$, $MoSe_2$, and $WSe_2$, Opt. Express **21**, 4908 (2013).

[17] S. Tongay, J. Zhou, C. Ataca, K. Lo, T. S. Matthews, J. Li, J. C. Grossman, and J. Wu, Thermally driven crossover from indirect toward direct bandgap in 2D semiconductors: $MoSe_2$ versus $MoS_2$, Nano Lett. **12**, 5576 (2012).

[18] T. Venanzi, M. Selig, S. Winnerl, A. Pashkin, A. Knorr, M. Helm, and H. Schneider, Terahertz-induced energy transfer from hot carriers to trions in a $MoSe_2$ monolayer, ACS Photonics **8**, 2931 (2021).

[19] A. Eftekhari, Molybdenum diselenide ($MoSe_2$) for energy storage, catalysis, and optoelectronics, Appl. Mater. Today **8**, 1 (2017).

[20] P. J. Ko, A. Abderrahmane, N.-H. Kim, and A. Sandhu, High-performance near-infrared photodetector based on nano-layered $MoSe_2$, Semicond. Sci. Technol. **32**, 065015 (2017).

[21] S. Kumar and U. Schwingenschlogl, Thermoelectric response of bulk and monolayer $MoSe_2$ and $WSe_2$, Chem. Mater. **27**, 1278 (2015).

[22] M. Bernardi, M. Palummo, and J. C. Grossman, Extraordinary sunlight absorption and one nanometer thick photovoltaics using two-dimensional monolayer materials, Nano Lett. **13**, 3664 (2013).

[23] S. Poncé, F. Macheda, E. R. Margine, N. Marzari, N. Bonini, and F. Giustino, First-principles predictions of Hall and drift mobilities in semiconductors, Phys. Rev. Research **3**, 043022 (2021).

[24] F. Macheda, S. Poncé, F. Giustino, and N. Bonini, Theory and computation of Hall scattering factor in graphene, Nano Lett. **20**, 8861 (2020).

[25] F. Macheda, P. Barone, and F. Mauri, Frohlich electron-phonon interaction and LO-TO splitting in doped semiconductors, arXiv:2202.02835.

[26] T. Sekine, M. Izumi, T. Nakashizu, K. Uchinokura, and E. Matsuura, Raman scattering and infrared reflectance in 2*H*-$MoSe_2$, J. Phys. Soc. Jpn. **49**, 1069 (1980).

[27] P. Soubelet, A. E. Bruchhausen, A. Fainstein, K. Nogajewski, and C. Faugeras, Resonance effects in the Raman scattering of monolayer and few-layer $MoSe_2$, Phys. Rev. B **93**, 155407 (2016).

[28] D. Nam, J.-U. Lee, and H. Cheong, Excitation energy dependent Raman spectrum of $MoSe_2$, Sci. Rep. **5**, 17113 (2015).

[29] K. Kim, J.-U. Lee, D. Nam, and H. Cheong, Davydov splitting and excitonic resonance effects in Raman spectra of few-layer $MoSe_2$, ACS Nano **10**, 8113 (2016).

[30] A. Mooradian and G. Wright, First order Raman effect in III–V compounds, Solid State Commun. **4**, 431 (1966).

[31] S. Grimme, J. Antony, S. Ehrlich, and H. Krieg, A consistent and accurate ab initio parametrization of density functional dispersion correction (DFT-D) for the 94 elements H–Pu, J. Chem. Phys. **132**, 154104 (2010).

[32] H.-g. Kim and H. J. Choi, Thickness dependence of work function, ionization energy, and electron affinity of Mo and W dichalcogenides from DFT and *GW* calculations, Phys. Rev. B **103**, 085404 (2021).

[33] S. Baroni, S. De Gironcoli, A. Dal Corso, and P. Giannozzi, Phonons and related crystal properties from density-functional perturbation theory, Rev. Mod. Phys. **73**, 515 (2001).

[34] P. Giannozzi, S. Baroni, N. Bonini, M. Calandra, R. Car, C. Cavazzoni, D. Ceresoli, G. L. Chiarotti, M. Cococcioni, I. Dabo *et al.*, QUANTUM ESPRESSO: A modular and open-source software project for quantum simulations of materials, J. Phys.: Condens. Matter **21**, 395502 (2009).

[35] A. Zanatta, Revisiting the optical bandgap of semiconductors and the proposal of a unified methodology to its determination, Sci. Rep. **9**, 11225 (2019).

[36] P. Makuła, M. Pacia, and W. Macyk, How to correctly determine the band gap energy of modified semiconductor photocatalysts based on UV–Vis spectra, J. Phys. Chem. Lett. **9**, 6814 (2018).

[37] I. Pelant and J. Valenta, *Luminescence Spectroscopy of Semiconductors* (Oxford University Press, Oxford, 2012).

[38] I. Niehues, P. Marauhn, T. Deilmann, D. Wigger, R. Schmidt, A. Arora, S. M. de Vasconcellos, M. Rohlfing, and R. Bratschitsch, Strain tuning of the Stokes shift in atomically thin semiconductors, Nanoscale **12**, 20786 (2020).

[39] Y. Kanemitsu and S. Okamoto, Phonon structures and Stokes shift in resonantly excited luminescence of silicon nanocrystals, Phys. Rev. B **58**, 9652 (1998).

[40] E. Martin, C. Delerue, G. Allan, and M. Lannoo, Theory of excitonic exchange splitting and optical Stokes shift in silicon

nanocrystallites: Application to porous silicon, Phys. Rev. B **50**, 18258 (1994).

[41] J. Potts, C. T. Walker, and I. R. Nair, Temperature dependence of second-order Raman scattering in potassium and rubidium halides, Phys. Rev. B **8**, 2756 (1973).

[42] W. Windl, P. Pavone, K. Karch, O. Schütt, D. Strauch, P. Giannozzi, and S. Baroni, Second-order Raman spectra of diamond from *ab initio* phonon calculations, Phys. Rev. B **48**, 3164 (1993).

[43] P. Klein, H. Masui, J.-J. Song, and R. Chang, Selective resonant enhancement in the two-phonon Raman spectrum of Si and GaP, Solid State Commun. **14**, 1163 (1974).

[44] R. Coehoorn, C. Haas, J. Dijkstra, C. J. F. Flipse, R. A. de Groot, and A. Wold, Electronic structure of $MoSe_2$, $MoS_2$, and $WSe_2$. I. Band-structure calculations and photoelectron spectroscopy, Phys. Rev. B **35**, 6195 (1987).

[45] J. Chen and C. Wang, Second order Raman spectrum of $MoS_2$, Solid State Commun. **14**, 857 (1974).

[46] K. Gołasa, M. Grzeszczyk, P. Leszczyński, C. Faugeras, A. Nicolet, A. Wysmołek, M. Potemski, and A. Babiński, Multiphonon resonant Raman scattering in $MoS_2$, Appl. Phys. Lett. **104**, 092106 (2014).

[47] K. Gołasa, M. Grzeszczyk, R. Bożek, P. Leszczyński, A. Wysmołek, M. Potemski, and A. Babiński, Resonant Raman scattering in $MoS_2$—from bulk to monolayer, Solid State Commun. **197**, 53 (2014).

[48] A. Stacy and D. Hodul, Raman spectra of IVB and VIB transition metal disulfides using laser energies near the absorption edges, J. Phys. Chem. Solids **46**, 405 (1985).

[49] G. L. Frey, R. Tenne, M. J. Matthews, M. S. Dresselhaus, and G. Dresselhaus, Raman and resonance Raman investigation of $MoS_2$ nanoparticles, Phys. Rev. B **60**, 2883 (1999).

[50] B. Chakraborty, H. R. Matte, A. Sood, and C. Rao, Layer-dependent resonant Raman scattering of a few layer $MoS_2$, J. Raman Spectrosc. **44**, 92 (2013).

[51] See Supplemental Material at http://link.aps.org/supplemental/10.1103/PhysRevB.106.085204 for more information regarding the experimental details and additional analysis.

[52] J. Kopaczek, S. Zelewski, K. Yumigeta, R. Sailus, S. Tongay, and R. Kudrawiec, Temperature dependence of the indirect gap and the direct optical transitions at the high-symmetry point of the Brillouin zone and band nesting in $MoS_2$, $MoSe_2$, $MoTe_2$, $WS_2$, and $WSe_2$ crystals, J. Phys. Chem. C **126**, 5665 (2022).

[53] A. A. Mitioglu, P. Plochocka, G. Deligeorgis, S. Anghel, L. Kulyuk, and D. K. Maude, Second-order resonant Raman scattering in single-layer tungsten disulfide $WS_2$, Phys. Rev. B **89**, 245442 (2014).

[54] F. Macheda and N. Bonini, Magnetotransport phenomena in *p*-doped diamond from first principles, Phys. Rev. B **98**, 201201(R) (2018).

[55] See https://research.csc.fi/-/mahti.